nature photonics

Article

https://doi.org/10.1038/s41566-023-01318-6

Three-dimensional nonlinear optical materials from twisted two-dimensional van der Waals interfaces

Received: 22 February 2023

Accepted: 21 September 2023

Bumho Kim[1], Jicheng Jin[1], Zhi Wang[1], Li He[1], Thomas Christensen[2,3], Eugene J. Mele[1] & Bo Zhen[1]

To enable new nonlinear responses, metamaterials are created by organizing structural units (meta-atoms), which are typically on the scale of about a hundred nanometres. However, truly altering the atomic symmetry and enabling new nonlinear responses requires control at the atomic scale, down to a few ångströms. Here we report three-dimensional nonlinear optical materials realized by the precise control and twist of individual two-dimensional van der Waals interfaces. Specifically, new nonlinear crystals are achieved by adding pseudo-screw symmetries to a multiple of four-layer WS_2 stacks (for example, four layer, eight layer and so on). Nonlinear susceptibility and circular selectivity of the resulting three-dimensional crystals are fundamentally different from natural WS_2, demonstrating a microscopic analogue to the fabrication of metamaterials with unique optical properties. Furthermore, we show that the magnitude of the newly enabled nonlinearity is enhanced by controlling the number of interfaces and the excitation wavelength. Our findings suggest a new approach to redesign the intrinsic nonlinearity in artificial atomic configurations, scalable from a few-nanometre-thick unit cells to bulk materials.

Material responses to light are highly constrained by symmetry. For example, two photons of identical frequency incident on a material can excite second-harmonic (SH) polarization at double the frequency with an amplitude proportional to the allowed second-order nonlinear susceptibility components of the material. Meanwhile, these nonlinear components are constrained by the point group symmetry of the materials[1–5]. Crystalline three-dimensional (3D) materials have fixed intrinsic point group symmetries, which are often limited to naturally existing and stable phases of materials. Beyond natural materials, new nonlinear responses have been enabled in metamaterials through symmetry control[6–9]. For instance, breaking the inversion symmetry at the surfaces of natural materials[10–12] or large-scale (~100 nm) meta-atoms[8,13–15] has enabled second-order nonlinear responses from inversion symmetric materials, where all second-order nonlinear susceptibility components are otherwise forbidden. Such new responses are mostly confined to the surfaces of materials, whereas the bulk mainly contributes to absorption losses[6,8,9,16]. As constituent meta-atoms inherently have low surface-to-volume ratios, current metamaterials typically have limited performances, such as overall frequency conversion efficiency, in practical applications[9,16–18].

Different from conventional approaches in 3D materials, the advent of twisted van der Waals (vdW) materials enables control over their intrinsic point group symmetries[19–22]. The modified symmetry of twisted vdW stacks, in turn, significantly affects the electronic wavefunction at the twisted interfaces and enables previously forbidden new nonlinear responses[23]. Although previous studies have focused on controlling nonlinear responses at a single twisted interface[23–27] or

---

[1]Department of Physics and Astronomy, University of Pennsylvania, Philadelphia, PA, USA. [2]Department of Physics, Massachusetts Institute of Technology, Cambridge, MA, USA. [3]Department of Electrical and Photonics Engineering, Technical University of Denmark, Kgs. Lyngby, Denmark. e-mail: bozhen@sas.upenn.edu

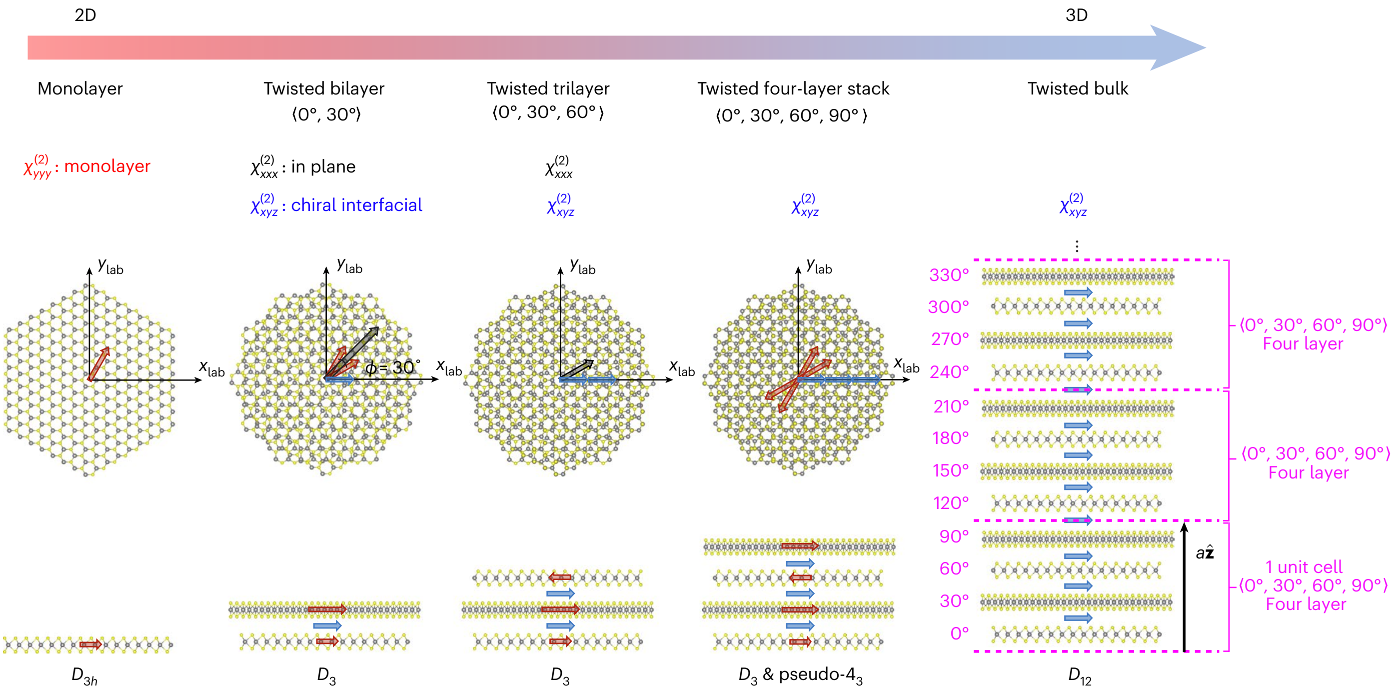

Fig. 1 | Redesigned second-order susceptibility in a twisted 3D crystal. Atomic structures and SH polarizations in different stacks, including a WS_2 monolayer (D_{3h} symmetry), a ⟨0°, 30°⟩ twisted bilayer stack (D_3 symmetry), a ⟨0°, 30°, 60°⟩ twisted trilayer stack (D_3 symmetry), a ⟨0°, 30°, 60°, 90°⟩ four-layer stack (D_3 symmetry and pseudo-4_3) and a twisted bulk with a fixed twist angle of 30° (D_{12} symmetry) under y_{lab}- and z_{lab}-polarized excitation. The twisted bulk structure is equivalent to ⟨0°, 30°, 60°, 90°⟩ four layers stacked along the $\hat{z}$ direction. Representative allowed second-order susceptibility elements ($\chi^{(2)}_{ijk}$) by various symmetries are listed for each stack (Supplementary Table 1). Twisted four-layer and bulk structures only allow chiral interfacial nonlinear susceptibility ($\chi^{(2)}_{xyz}$) whose SH polarizations are denoted by blue arrows. SH polarizations along an armchair direction of each monolayer are denoted by the red arrows whose sum is denoted by the black arrow. The grey and yellow circles represent tungsten and sulfur atoms, respectively.

a few twisted interfaces with a low interface-to-volume ratio[28], here we demonstrate a 3D crystal, completely made of twisted two-dimensional (2D) interfaces. In contrast to conventional metamaterials, our 3D crystal exhibits new interfacial nonlinear responses throughout its bulk. Overall, our study opens a new path to redesign the optical nonlinearities of 3D materials at the microscopic scale by stacking and controlling individual 2D interfaces and promises new nonlinear functionalities for a broad range of applications including frequency conversion[29,30], bioimaging[31,32], ultrafast photonics[33,34], quantum computing[21,35] and communication[36,37].

Theory for nonlinear twisted 3D crystals

In this section, we introduce a new approach to build nonlinear 3D crystals from twisted 2D interfaces (Fig. 1). We start by discussing nonlinear responses of monolayer and twisted bilayer WS_2 based on their symmetries. A WS_2 monolayer belongs to the D_{3h} point group, which supports second-order susceptibility elements[1,2,5] of $\chi^{(2)}_{yyy} = -\chi^{(2)}_{yxx}$ and enables an SH polarization along the armchair direction (Fig. 1, red arrow). On stacking two monolayers at a generic twist angle ($\phi \neq 0°$ and 180°), the point group is reduced from D_{3h} (monolayer) to D_3 (twisted bilayer) due to the breaking of mirror symmetries[19–22]. The twisted bilayers have both in-plane ($\chi^{(2)}_{xxx} = -\chi^{(2)}_{xyy}$) and interfacial ($\chi^{(2)}_{xyz} = -\chi^{(2)}_{yxz}$) second-order susceptibility elements. Although the former response (black arrow) is the sum of amplitudes from individual monolayer responses (red arrows), the latter response (blue arrow) is a new chiral response arising from broken mirror symmetries (Fig. 1). In particular, this interfacial nonlinear response does not come from either layer separately but is a cooperative effect originating from the coupling between the electronic wavefunctions from the two layers[23].

Further analysis of this interfacial nonlinear susceptibility $\chi^{(2)}_{xyz}$ reveals two interesting properties. First, when the sample rotates in plane, the interfacial SH polarization always points to a fixed direction, whereas the in-plane (and monolayer) SH polarization rotates with the sample (Supplementary Fig. 1). For instance, when a twisted stack is tilted by β around the lab x axis, a vertically polarized excitation can generate horizontal in-plane SH polarization ($\propto \chi^{(2)}_{xxx}\cos^2\beta\cos 3\theta$), sensitive to in-plane sample orientation θ (Supplementary Section III). Meanwhile, interfacial SH polarization ($\propto \chi^{(2)}_{xyz}\sin 2\beta$) is independent of the in-plane sample orientation and always points to the horizontal direction. Furthermore, $\chi^{(2)}_{xyz}$ strongly depends on the relative twist angle of the top layer with respect to the bottom (ϕ). The sign of $\chi^{(2)}_{xyz}$ flips when the twist angle is reversed: $\chi^{(2)}_{xyz}(\phi) = -\chi^{(2)}_{xyz}(-\phi)$. Supplementary Fig. 3 provides more details and Fig. 2e shows our experimental demonstration.

Twisted trilayer samples can be similarly analysed as two twisted interfaces: one between the bottom layer and the middle, and the other between the middle and the top. For example, a trilayer stack in the ⟨0°, 30°, 60°⟩ configuration has two twisted interfaces, both at +30°, creating identical interfacial SH polarizations that constructively add up. On the other hand, a trilayer stack in the ⟨0°, 30°, 0°⟩ configuration has two oppositely twisted interfaces, one at +30° and the other at −30°. The opposite interfacial SH polarizations cancel out any chiral responses, which is consistent with the preserved up–down mirror symmetry of the stack.

In particular, screw symmetry emerges in a twisted four-layer stack in the ⟨0°, 30°, 60°, 90°⟩ configuration. Specifically, all interfacial SH polarizations (blue arrows) add up, whereas in-plane SH polarizations from individual layers (red arrows) exactly cancel between the first (second) layer and the third (fourth) layer as they point in opposite directions (Fig. 1). Altogether, the four-layer stack only allows chiral

https://doi.org/10.1038/s41566-023-01318-6

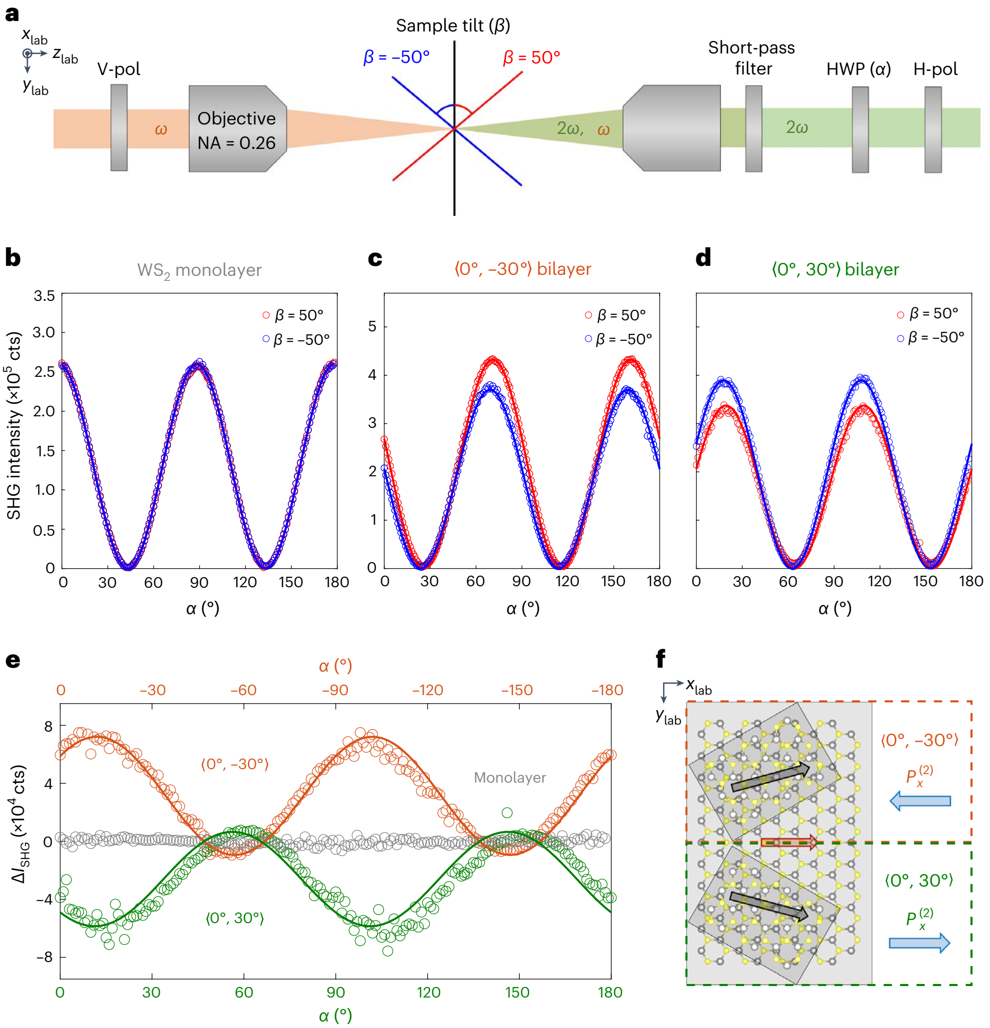

Fig. 2 | Interfacial nonlinear susceptibility in twisted bilayer WS$_2$. **a**, SHG measurement setup to characterize both individual layer and interfacial nonlinear responses (Methods). V-pol (H-pol) denotes a vertical (horizontal) polarizer along the y (x) direction. NA, numerical aperture. **b**–**d**, SHG signals are measured at the two incidence angles, namely, $\beta = 50°$ (red) and $\beta = -50°$ (blue), on different devices, including monolayer (**b**) and ⟨0°, −30°⟩ (**c**) and ⟨0°, 30°⟩ (**d**) bilayer stacks. The rotation angle of the half-wave plate (HWP) is denoted as α. **e**, Differences in the SHG signals (ΔI_{SHG}) between the incidence angles of $\beta = \pm 50°$ of a monolayer (grey), ⟨0°, 30°⟩ bilayer (green) and ⟨0°, −30°⟩ bilayer (orange circles). The solid lines in **b**–**d** and **e** are the best-fit curves from symmetry analysis (equation (1) and Supplementary Equation (14), respectively). **f**, Schematic of ⟨0°, ±30°⟩ bilayer stacks, mirror symmetric to each other, inducing oppositely aligned interfacial SH polarizations ($P_x^{(2)}$, blue arrows).

interfacial susceptibility ($\chi^{(2)}_{xyz}$) that is different from the D_3 point group constraints in twisted bilayers and trilayers (Supplementary Table 1). This emerging constraint can be understood by a pseudo-4_3 screw symmetry that forbids in-plane susceptibility $\chi^{(2)}_{xxx}$ (Supplementary Section I). Such an artificially added screw symmetry opens new paths to engineer 3D symmetries and nonlinearities of vdW stacks (Supplementary Section II).

The unconventional nonlinearities that we discovered in twisted four-layer stacks are preserved in the 3D bulk crystal limit, which is well understood by the new point group. Specifically, a twisted bulk with a twist angle of $\phi = 30°$ between any two adjacent layers belongs to the D_{12} point group. Applying Neumann's principle to the less understood D_{12} point group, our theoretical analysis shows that only chiral susceptibility components, $\chi^{(2)}_{xyz}$, are allowed, whereas all in-plane susceptibility components (for example, $\chi^{(2)}_{xxx}$ and $\chi^{(2)}_{yyy}$) are forbidden. This feature is consistent with a single four-layer twisted stack as we analysed before. The consistency can be intuitively understood as the bulk crystal is essentially a vertical stacking of the four-layer twisted stack. In other words, the four-layer twisted stack is the new unit cell of the twisted bulk crystal, so they support the same nonlinear susceptibility components.

Experimental demonstration

We perform second-harmonic generation (SHG) measurements to verify the predicted nonlinearities of twisted WS$_2$ in the various stacking configurations. Twisted WS$_2$ stacks, up to eight layers thick, are prepared on fused silica substrates using the 'tear and stack' method[38,39] (Methods). In contrast to SHG under normal excitation only arising from in-plane responses, we measure SHG under oblique incident angles (β) set to be either +50° and −50° to observe both in-plane and interfacial nonlinear responses (Fig. 2a and Methods). A monolayer shows identical SHG signals between $\beta = 50°$ (Fig. 2b, red circles) and −50° (blue circles). This result indicates that the in-plane SH responses from the monolayer are independent of the opposite incident angle, which is also consistent with theoretical modelling based on the D_{3h} point group (Fig. 2b, solid line).

In contrast, twisted bilayers, belonging to the D_3 point group, create SH polarizations in two ways: through the in-plane layer responses

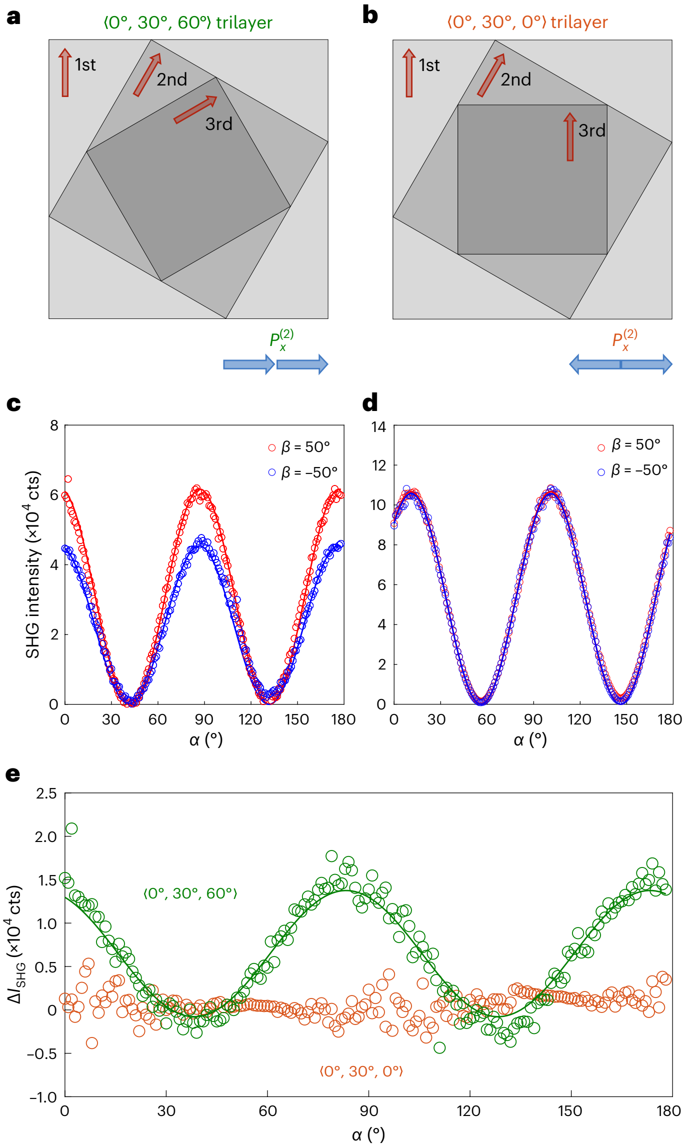

Fig. 3 | Scalability of interfacial nonlinear susceptibility in twisted trilayer WS$_2$ stacks. a,**b**, Schematic of SH polarizations from interfaces (blue arrows) and individual layers (red arrows) in ⟨0°, 30°, 60°⟩ (**a**) and ⟨0°, 30°, 0°⟩ (**b**) trilayer stacks. The interfacial SH polarizations interfere constructively and add up in **a**, but interfere destructively and cancel in **b**. **c**,**d**, Measured SHG signals under an incidence angle of $\beta = 50°$ ($\beta = -50°$) are shown in red (blue) circles for ⟨0°, 30°, 60°⟩ (**c**) and ⟨0°, 30°, 0°⟩ (**d**) stacks. **e**, Difference in SHG intensity between the incidence angles of $\beta = \pm 50°$ shows vanishing (orange) and enhanced (green) interfacial susceptibility in the ⟨0°, 30°, 0°⟩ and ⟨0°, 30°, 60°⟩ stacks.

and the interfacial responses producing a net SHG intensity (Supplementary Section III).

$$I_{\mathrm{SHG}} \propto \left(-\chi^{(2)}_{\mathrm{s},xxx}\cos^2\beta\left(\cos 2\alpha\cos 3\theta + \cos\beta\sin 2\alpha\sin 3\theta\right) + \chi^{(2)}_{\mathrm{s},xyz}\sin 2\beta\cos 2\alpha\right)^2, \qquad (1)$$

where $\chi^{(2)}_{\mathrm{s},xxx}$ and $\chi^{(2)}_{\mathrm{s},xyz}$ are the in-plane and interfacial sheet susceptibility elements, respectively. The SHG intensity is proportional to the square of the SH polarizations from individual layers (the $\chi^{(2)}_{\mathrm{s},xxx}$ term in equation (1)) and the interface (the $\chi^{(2)}_{\mathrm{s},xyz}$ term). Unlike the monolayer example, the observed SHG signal is generally stronger for $\beta = 50°$ than $\beta = -50°$ for the ⟨0°, −30°⟩ bilayer stack (Fig. 2c); conversely, the opposite trend is observed for the ⟨0°, 30°⟩ bilayer stack (Fig. 2d). Specifically, under the two oblique incidences ($\beta = \pm 50°$), the in-plane SH polarizations ($\chi^{(2)}_{\mathrm{s},xxx}$) are identical, whereas the interfacial SH polarizations ($\chi^{(2)}_{\mathrm{s},xyz}$) are exactly opposite (equation (1)). The clear difference in SHG signals under the two opposite incident angles evinces the interfacial response of the twisted bilayers.

Next, we examine the interfacial responses of bilayer samples with opposite twist angles, namely, $\phi = \pm 30°$, in more detail. Following equation (1), the difference between SHG signals, $\Delta I_{\mathrm{SHG}} = I(\beta = +50°) - I(\beta = -50°)$, is proportional to the interfacial sheet susceptibility $\chi^{(2)}_{\mathrm{s},xyz}$. The ⟨0°, 30°⟩ (Fig. 2e, green circles) and ⟨0°, −30°⟩ (orange circles) bilayer stacks have ΔI_{SHG} of approximately equal magnitude but opposite signs. Using our theoretical model (green and orange solid lines; see Supplementary Section IV for details), we extract $\chi^{(2)}_{\mathrm{s},xyz,\mathrm{norm}} = 0.027$ for the ⟨0°, 30°⟩ stack and $\chi^{(2)}_{\mathrm{s},xyz,\mathrm{norm}} = -0.031$ for the ⟨0°, −30°⟩ stack. Both values are normalized to the monolayer sheet susceptibility (Supplementary Section V). This result is consistent with our earlier prediction $\chi^{(2)}_{xyz}(\phi) = -\chi^{(2)}_{xyz}(-\phi)$, namely, the interfacial SH polarization reverses its direction when the twist angle is reversed (Fig. 2f).

We next examine the scalability of interfacial responses by measuring a trilayer stack in the ⟨0°, 30°, 60°⟩ configuration. Figure 3a shows a schematic of interfacial SH polarizations (blue arrows) pointing to the same direction and adding up. The observed SHG signals from the trilayer show a significant difference between $\beta = 50°$ and $-50°$, indicating finite interfacial responses (Fig. 3c,e). The observed ΔI_{SHG} (Fig. 3e, circles) is consistent with our theoretical model (solid line), which yields $\chi^{(2)}_{\mathrm{s},xyz,\mathrm{norm}} \approx 0.042$, exceeding the corresponding response in the ⟨0°, 30°⟩ bilayer stack ($\chi^{(2)}_{\mathrm{s},xyz,\mathrm{norm}} = 0.027$). We further show that the interfacial SH field amplitude linearly scales with the sample thickness within the experimental uncertainty (Fig. 4f). This experimental observation agrees well with our theory prediction: the interfacial nonlinear responses coherently add up when interfacial twist angles are the same. This stacking sequence is different from the widely studied 3R-type stacks ($\phi = 0°$) where the in-plane layer nonlinear responses coherently add up[28,40]. To further validate the origin of the differences in SHG, we examine a trilayer in the ⟨0°, 30°, 0°⟩ configuration with two oppositely twisted interfaces (Fig. 3b). Figure 3d,e shows the SHG signals with almost no difference at the incident angles between $\beta = 50°$ and $-50°$, implying a negligible net interfacial response: $\chi^{(2)}_{\mathrm{s},xyz} \approx 0$, which results from the cancellation between the two opposite interfacial SH polarizations, as we predicted. The contrasting results between the two trilayers with the same constituent layers but different interfaces confirm that the observed ΔI_{SHG} value originates from vdW interfaces.

We experimentally demonstrate the unconventional susceptibility ($\chi^{(2)}_{\mathrm{s},xxx} = 0$ and $\chi^{(2)}_{\mathrm{s},xyz} \neq 0$) of a twisted four-layer-unit-cell structure. We first measure the in-plane response, $\chi^{(2)}_{xxx}$, of the four-layer stack under normal excitation ($\beta = 0°$), where we observe a substantially reduced response (Fig. 4b, purple) relative to the monolayer (grey). SHG spatial maps further confirm the strong suppression of $\chi^{(2)}_{\mathrm{s},xxx}$ of twisted four-layer stacks (Supplementary Fig. 6), consistent with the presence of pseudo-4_3 screw symmetry. Figure 4c shows stronger SHG signals in oblique-excitation measurements ($\beta = \pm 50°$) compared with the normal-incidence measurements ($\beta = 0°$). This is direct evidence of stronger interfacial sheet susceptibility than in-plane sheet susceptibility in the twisted four-layer stack, which agrees with our previous theoretical prediction. Moreover, the nearly identical SHG signals at the two opposite incident angles are consistent with the sheet susceptibility of the four-layer stack: $\chi^{(2)}_{\mathrm{s},xxx} = 0$ and $\chi^{(2)}_{xyz} \neq 0$ (equation (1)). In particular, the intrinsic nonlinearities of the four-layer stack are the same as those of some 3D materials (such as TeO$_2$ (ref. 41) and La$_4$InSbS$_9$ (ref. 42)), but fundamentally different from those of previously studied natural and twisted 2D materials (Supplementary Table 2). Our approach of engineering electronic wavefunction symmetries completely alters the intrinsic nonlinearity at the microscopic scale, which substantially reduces the required feature size (~100 nm) in

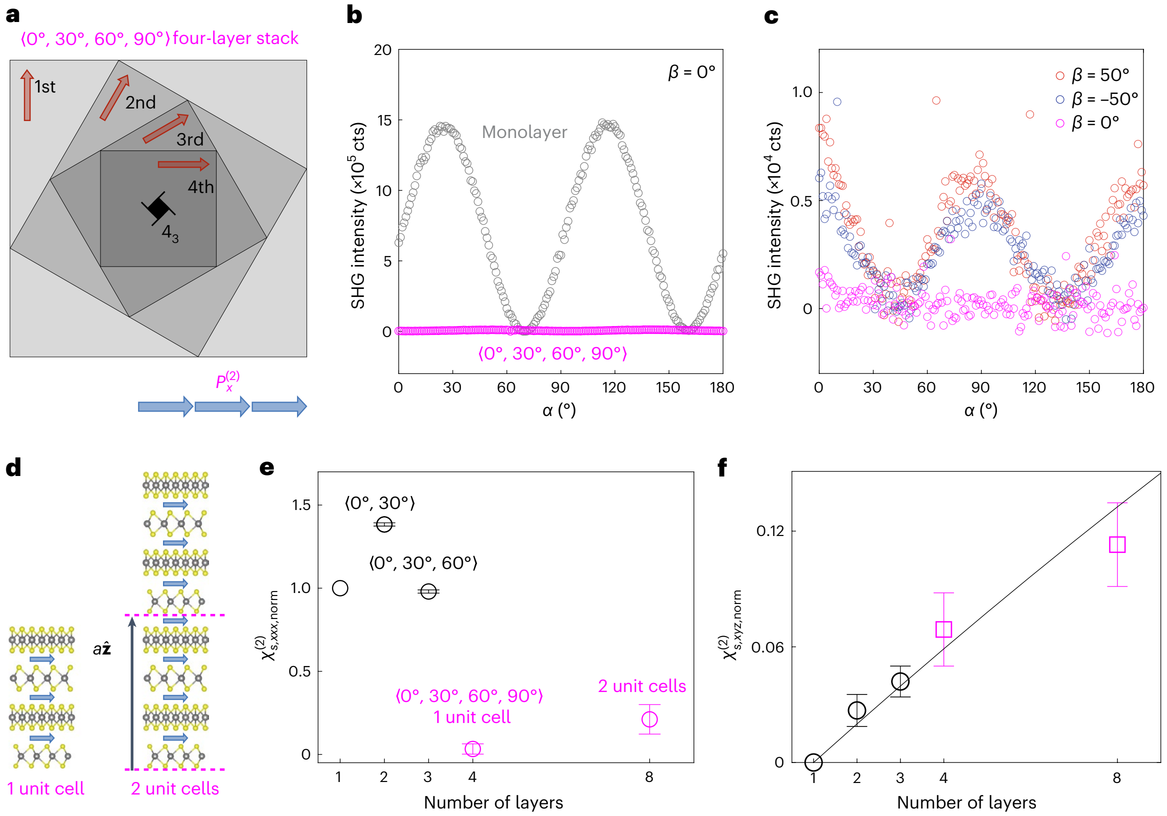

Fig. 4 | Scalable nonlinear optical material. a, Pseudo-four-fold screw symmetry (4_3) in four-layer WS_2 forbids in-plane SH polarizations (red arrows) whereas all of the interfacial SH polarizations (blue arrows) are added. **b**, SHG signals under normal excitation show a significant suppression of in-plane responses in a four-layer stack (purple), compared with a monolayer (grey). **c**, SHG signals from the four-layer stack under the incidence angles of 50° (red), 0° (purple) and −50° (blue). **d**, Schematic of a twisted four-layer stack as a scalable nonlinear optical material unit cell that can be stacked along the $\hat{z}$ direction. **e**,**f**, Four and eight layers with screw symmetry have suppressed normalized in-plane sheet susceptibility, $\chi^{(2)}_{s,xxx,norm}$ (**e**), and enhanced normalized interfacial sheet susceptibility, $\chi^{(2)}_{s,xyz,norm}$ (**f**), linearly with the number of stack layers. Data for 2–8 layers represent the mean values ± standard deviations (s.d.), extracted from two different spots on each sample. Methods provides the measurement details.

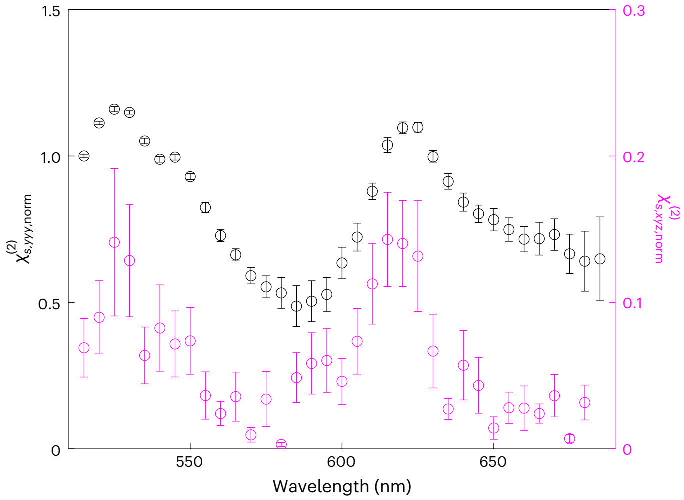

Fig. 5 | Enhanced nonlinear susceptibility by exciton resonances. Normalized in-plane sheet susceptibility, $\chi^{(2)}_{s,yyy,norm}$, from a monolayer (black circles) and interfacial sheet susceptibility, $\chi^{(2)}_{s,xyz,norm}$, from a twisted four-layer stack (purple circles), are both enhanced when the SH frequency is on resonance with excitons. Data represent values extracted from one spot of each sample where the error bars represent uncertainties estimated by the s.d. of intensity noise over the measured spectra.

conventional nonlinear optical metamaterials[43,44]. Moreover, we observe chiral Raman scattering from our twisted stacks (Supplementary Section VIII), implying that broken mirror symmetries at interfaces promise diverse chiroptical responses such as circular dichroism[45,46] and circular birefringence[47].

To scale up a four-layer unit cell into a 3D crystal, we experimentally verify the nonlinearities of a vertical stack of two four-layer unit cells (Fig. 4d). Our experimental results show a strong suppression of $\chi^{(2)}_{s,xxx}$ (Fig. 4e) and an even further enhancement in $\chi^{(2)}_{s,xyz}$ (Fig. 4f) in the twisted eight-layer stack, consisting of two four-layer unit cells. Although strongly suppressed, $\chi^{(2)}_{s,xxx}$ is increased relative to the four-layer stack, which might be caused by the reabsorption of SHG from each layer as well as imperfect twist-angle alignment (Supplementary Section VI and Supplementary Table 3). Meanwhile, interfacial SH field amplitude ($\propto \chi^{(2)}_{s,xyz}$) scales approximately linearly with the sample thickness, which is consistent with our theoretical model incorporating interference and reabsorption effects (Fig. 4f, solid line). Our observation promises even stronger interfacial responses in thicker samples by simply stacking four-layer unit cells together. Moreover, the interfacial nonlinearity can also be further enhanced by the excitonic resonance effect (Fig. 5). The in-plane sheet susceptibility of a monolayer has two prominent peaks at the A-exciton (~620 nm) and B-exciton (~525 nm) wavelengths, known as the exciton-enhanced SHG[48,49]. The excitonic resonance effect is also observed in the interfacial sheet susceptibility of four-layer WS_2, reaching $\chi^{(2)}_{s,xyz,norm} \approx 0.14$,

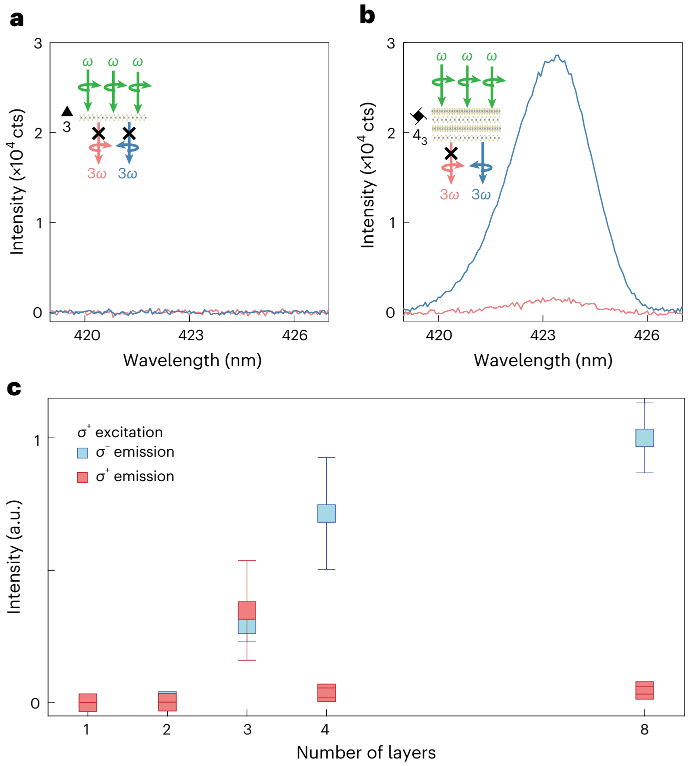

Fig. 6 | Nonlinear circular selectivity enabled by a four-fold screw symmetry. **a**, Monolayer with three-fold rotational symmetry forbids THG under circularly polarized excitation. **b**, A ⟨0°, 30°, 60°, 90°⟩ four-layer stack with a pseudo-four-fold screw symmetry converts right-circularly polarized excitation into left-circularly polarized THG. **c**, Helicity-resolved THG intensity as a function of layer number. All interlayer twist angles are +30°. Data for three-, four- and eight-layer stacks represent mean values ± s.d., extracted from five, seven and five different spots on each sample, respectively. Data of one- and two-layer stacks represent values extracted from one spot of each sample, where the error bars represent uncertainties estimated by the s.d. of intensity noise over the measured spectra.

which is over three times higher than the off-resonance value. Moreover, we theoretically suggest an approach to achieve quasi-phase matching in a thick 3D twisted stack, which promises strong interfacial responses (Supplementary Section IX).

Finally, we discover emerging nonlinear circular selectivity enabled by the artificially added screw symmetry. In a monolayer WS_2 (Fig. 6a), third-harmonic generation (THG) is not observed under circularly polarized excitation. This is consistent with the circular selection rule from the D_{3h} point group of a monolayer (Supplementary Section X). Meanwhile, right-circularly polarized (σ^+) excitation at the frequency of ω produces left-circularly polarized (σ^-) THG at the frequency of 3ω in a twisted four-layer structure (Fig. 6b). The counter-circularly polarized THG is typically produced by materials with a four-fold symmetry[50–52], where the lattice symmetry provides the mismatched angular momentum between the input and output photons.

To better understand the emerging circular selectivity, we performed the helicity-resolved THG measurements for twisted WS_2 stacks with different layer numbers and symmetries (Fig. 6c). The circularly polarized THG intensity increases with the twisted stack thickness. The production of THG implies broken three-fold symmetry that has been often observed in twisted stacks due to the strain effect[53–55]. Indeed, the observed THG from the individual twisted stacks can be well understood by taking into account the strain effect as well as their symmetries (Supplementary Section X). We predict that twisted bilayer and trilayer can have mixed left- and right-circularly polarized THG, consistent with the observed THG. Meanwhile, twisted four- and eight-layer stacks with the four-fold screw symmetry show THG with near-unity polarization of ~90% and ~91%, respectively. This sharp rise in the polarization conversion efficiency in the twisted four-layer configuration provides strong evidence that the four-fold screw symmetry is required for the emerging circular selectivity. Intuitively, this effect can be understood by angular momentum conservation enabled by the artificial four-fold screw symmetry, which promises to control nonlinear selectivity through a proper selection of intrinsic and artificial symmetries.

Discussion

To conclude, we directly engineer the symmetries of electronic wavefunctions by stacking individual monolayers into a precisely designed 3D configuration. Compared with conventional optical metamaterials composed of meta-atoms on the scale of ~100 nm (refs. 8,43,44), our approach suggests a new path to engineer optical nonlinearity at the microscopic scale down to a few nanometres. Our engineered stacks show completely redesigned nonlinear susceptibility as well as circular selectivity, which takes us one step closer to the designing of intrinsic nonlinearities at will. The newly enabled chiral nonlinearities could be applied to a broad range of photonic device applications to harness spin angular momentum of light[56–60]. Furthermore, stacking monolayers with a screw symmetry can enable various quasi-crystals, providing a practical platform to explore their emerging nonlinearity. Our approach to control symmetries can be readily extended to other physical responses that are also sensitive to material symmetries including elasticity, thermal expansion and piezoelectricity[61–64].

Online content

Any methods, additional references, Nature Portfolio reporting summaries, source data, extended data, supplementary information, acknowledgements, peer review information; details of author contributions and competing interests; and statements of data and code availability are available at https://doi.org/10.1038/s41566-023-01318-6.

References

1. Boyd, R. W. *Nonlinear Optics* 3rd edn (Academic, 2008).
2. Sutherland, R. L., McLean, D. G. & Kirkpatrick, S. *Handbook of Nonlinear Optics* 2nd edn (Marcel Dekker, 2003).
3. Bergfeld, S. & Daum, W. Second-harmonic generation in GaAs: experiment versus theoretical predictions of $\chi^{(2)}_{xyz}$. *Phys. Rev. Lett.* **90**, 036801 (2003).
4. Wu, L. et al. Giant anisotropic nonlinear optical response in transition metal monopnictide Weyl semimetals. *Nat. Phys.* **13**, 350–355 (2017).
5. Li, Y. et al. Probing symmetry properties of few-layer MoS_2 and h-BN by optical second-harmonic generation. *Nano Lett.* **13**, 3329–3333 (2013).
6. Kauranen, M. & Zayats, A. V. Nonlinear plasmonics. *Nat. Photon.* **6**, 737–748 (2012).
7. Lapine, M., Shadrivov, I. V. & Kivshar, Y. S. Colloquium: nonlinear metamaterials. *Rev. Mod. Phys.* **86**, 1093–1123 (2014).
8. Li, G., Zhang, S. & Zentgraf, T. Nonlinear photonic metasurfaces. *Nat. Rev. Mater.* **2**, 17010 (2017).
9. Kadic, M., Milton, G. W., van Hecke, M. & Wegener, M. 3D metamaterials. *Nat. Rev. Phys.* **1**, 198–210 (2019).
10. Shen, Y. R. Surface properties probed by second-harmonic and sum-frequency generation. *Nature* **337**, 519–525 (1989).
11. Guyot-Sionnest, P. & Shen, Y. R. Local and nonlocal surface nonlinearities for surface optical second-harmonic generation. *Phys. Rev. B* **35**, 4420–4426 (1987).
12. Cazzanelli, M. & Schilling, J. Second order optical nonlinearity in silicon by symmetry breaking. *Appl. Phys. Rev.* **3**, 011104 (2016).

13. Lee, J. et al. Giant nonlinear response from plasmonic metasurfaces coupled to intersubband transitions. *Nature* **511**, 65–69 (2014).
14. Butet, J., Brevet, P.-F. & Martin, O. J. F. Optical second harmonic generation in plasmonic nanostructures: from fundamental principles to advanced applications. *ACS Nano* **9**, 10545–10562 (2015).
15. Linnenbank, H., Grynko, Y., Förstner, J. & Linden, S. Second harmonic generation spectroscopy on hybrid plasmonic/dielectric nanoantennas. *Light: Sci. Appl.* **5**, e16013 (2016).
16. Khurgin, J. B. How to deal with the loss in plasmonics and metamaterials. *Nat. Nanotechnol.* **10**, 2–6 (2015).
17. Bonacina, L., Brevet, P.-F., Finazzi, M. & Celebrano, M. Harmonic generation at the nanoscale. *J. Appl. Phys.* **127**, 230901 (2020).
18. Valev, V. K. Characterization of nanostructured plasmonic surfaces with second harmonic generation. *Langmuir* **28**, 15454–15471 (2012).
19. Wu, F., Lovorn, T., Tutuc, E., Martin, I. & MacDonald, A. Topological insulators in twisted transition metal dichalcogenide homobilayers. *Phys. Rev. Lett.* **122**, 086402 (2019).
20. Angeli, M. & MacDonald, A. H. Γ valley transition metal dichalcogenide moiré bands. *Proc. Natl Acad. Sci. USA* **118**, e2021826118 (2021).
21. Zhang, Y., Liu, T. & Fu, L. Electronic structures, charge transfer, and charge order in twisted transition metal dichalcogenide bilayers. *Phys. Rev. B* **103**, 155142 (2021).
22. Zhou, B. T., Egan, S. & Franz, M. Moiré flat Chern bands and correlated quantum anomalous Hall states generated by spin-orbit couplings in twisted homobilayer MoS_2. *Phys. Rev. Res.* **4**, L012032 (2022).
23. Yang, F. et al. Tunable second harmonic generation in twisted bilayer graphene. *Matter* **3**, 1361–1376 (2020).
24. Hsu, W.-T. et al. Second harmonic generation from artificially stacked transition metal dichalcogenide twisted bilayers. *ACS Nano* **8**, 2951–2958 (2014).
25. Paradisanos, I. et al. Second harmonic generation control in twisted bilayers of transition metal dichalcogenides. *Phys. Rev. B* **105**, 115420 (2022).
26. van der Zande, A. M. et al. Tailoring the electronic structure in bilayer molybdenum disulfide via interlayer twist. *Nano Lett.* **14**, 3869–3875 (2014).
27. Liu, K. et al. Evolution of interlayer coupling in twisted molybdenum disulfide bilayers. *Nat. Commun.* **5**, 4966 (2014).
28. Yao, K. et al. Enhanced tunable second harmonic generation from twistable interfaces and vertical superlattices in boron nitride homostructures. *Sci. Adv.* **7**, eabe8691 (2021).
29. Koshelev, K. et al. Subwavelength dielectric resonators for nonlinear nanophotonics. *Science* **367**, 288–292 (2020).
30. Anthur, A. P. et al. Continuous wave second harmonic generation enabled by quasi-bound-states in the continuum on gallium phosphide metasurfaces. *Nano Lett.* **20**, 8745–8751 (2020).
31. Ray, P. C. Size and shape dependent second order nonlinear optical properties of nanomaterials and their application in biological and chemical sensing. *Chem. Rev.* **110**, 5332–5365 (2010).
32. Deka, G., Sun, C.-K., Fujita, K. & Chu, S.-W. Nonlinear plasmonic imaging techniques and their biological applications. *Nanophotonics* **6**, 31–49 (2017).
33. Hickstein, D. D. et al. Self-organized nonlinear gratings for ultrafast nanophotonics. *Nat. Photon.* **13**, 494–499 (2019).
34. Yu, W. et al. High-yield exfoliation of monolayer 1T′-$MoTe_2$ as saturable absorber for ultrafast photonics. *ACS Nano* **15**, 18448–18457 (2021).
35. Kwiat, P. G. et al. New high-intensity source of polarization-entangled photon pairs. *Phys. Rev. Lett.* **75**, 4337–4341 (1995).
36. Javerzac-Galy, C. et al. On-chip microwave-to-optical quantum coherent converter based on a superconducting resonator coupled to an electro-optic microresonator. *Phys. Rev. A* **94**, 053815 (2016).
37. Fan, L. et al. Superconducting cavity electro-optics: a platform for coherent photon conversion between superconducting and photonic circuits. *Sci. Adv.* **4**, eaar4994 (2018).
38. Kim, K. et al. van der Waals heterostructures with high accuracy rotational alignment. *Nano Lett.* **16**, 1989–1995 (2016).
39. Cao, Y. et al. Correlated insulator behaviour at half-filling in magic-angle graphene superlattices. *Nature* **556**, 80–84 (2018).
40. Liu, F. et al. Disassembling 2D van der Waals crystals into macroscopic monolayers and reassembling into artificial lattices. *Science* **367**, 903–906 (2020).
41. Okada, M., Takizawa, K. & Ieiri, S. The measurement of the antisymmetric components of nonlinear optical susceptibilities of TeO_2 crystal. *J. Appl. Phys.* **48**, 4163–4167 (1977).
42. Zhao, H.-J., Zhang, Y.-F. & Chen, L. Strong Kleinman-forbidden second harmonic generation in chiral sulfide: La_4InSbS_9. *J. Am. Chem. Soc.* **134**, 1993–1995 (2012).
43. Husu, H. et al. Metamaterials with tailored nonlinear optical response. *Nano Lett.* **12**, 673–677 (2012).
44. Czaplicki, R. et al. Enhancement of second-harmonic generation from metal nanoparticles by passive elements. *Phys. Rev. Lett.* **110**, 093902 (2013).
45. Byers, J. D., Yee, H. I., Petralli-Mallow, T. & Hicks, J. M. Second-harmonic generation circular-dichroism spectroscopy from chiral monolayers. *Phys. Rev. B* **49**, 14643–14647 (1994).
46. Belardini, A. et al. Circular dichroism in the optical second-harmonic emission of curved gold metal nanowires. *Phys. Rev. Lett.* **107**, 257401 (2011).
47. Ghosh, A. & Fischer, P. Chiral molecules split light: reflection and refraction in a chiral liquid. *Phys. Rev. Lett.* **97**, 173002 (2006).
48. Fan, X. et al. Mechanism of extreme optical nonlinearities in spiral WS_2 above the bandgap. *Nano Lett.* **20**, 2667–2673 (2020).
49. Seyler, K. L. et al. Electrical control of second-harmonic generation in a WSe_2 monolayer transistor. *Nat. Nanotechnol.* **10**, 407–411 (2015).
50. Chen, S. et al. Symmetry-selective third-harmonic generation from plasmonic metacrystals. *Phys. Rev. Lett.* **113**, 033901 (2014).
51. Zhang, C., Li, Z.-Q., Yang, X., Chen, Z. & Wang, Z. Controlling third harmonic generation with gammadion-shaped chiral metamaterials. *AIP Adv.* **6**, 125014 (2016).
52. Saito, N. et al. Observation of selection rules for circularly polarized fields in high-harmonic generation from a crystalline solid. *Optica* **4**, 1333–1336 (2017).
53. Kerelsky, A. et al. Maximized electron interactions at the magic angle in twisted bilayer graphene. *Nature* **572**, 95–100 (2019).
54. Kazmierczak, N. P. et al. Strain fields in twisted bilayer graphene. *Nat. Mater.* **20**, 956–963 (2021).
55. Ci, P. et al. Breaking rotational symmetry in supertwisted WS_2 spirals via moiré magnification of intrinsic heterostrain. *Nano Lett.* **22**, 9027–9035 (2022).
56. Sun, L. et al. Separation of valley excitons in a MoS_2 monolayer using a subwavelength asymmetric groove array. *Nat. Photon.* **13**, 180–184 (2019).
57. Shreiner, R., Hao, K., Butcher, A. & High, A. A. Electrically controllable chirality in a nanophotonic interface with a two-dimensional semiconductor. *Nat. Photon.* **16**, 330–336 (2022).
58. Lodahl, P. et al. Chiral quantum optics. *Nature* **541**, 473–480 (2017).
59. Zhang, Y. et al. Chirality logic gates. *Sci. Adv.* **8**, eabq8246 (2022).
60. Hu, G. et al. Coherent steering of nonlinear chiral valley photons with a synthetic Au-WS_2 metasurface. *Nat. Photon.* **13**, 467–472 (2019).

61. Newnham, R. E. *Properties of Materials: Anisotropy, Symmetry, Structure* (Oxford Univ. Press, 2004).
62. Hu, C., Wang, R. & Ding, D.-H. Symmetry groups, physical property tensors, elasticity and dislocations in quasicrystals. *Rep. Progr. Phys.* **63**, 1–39 (2000).
63. Duerloo, K.-A. N., Ong, M. T. & Reed, E. J. Intrinsic piezoelectricity in two-dimensional materials. *J. Phys. Chem. Lett.* **3**, 2871–2876 (2012).
64. Hu, L. et al. Localized symmetry breaking for tuning thermal expansion in ScF_3 nanoscale frameworks. *J. Am. Chem. Soc.* **140**, 4477–4480 (2018).

Methods

Sample preparation

A gold tape was prepared following the detailed procedures in the previous study[40]. A 150-nm-thick gold film on SiO_2/Si substrates was coated with polyvinylpyrrolidone and then picked up by a thermal release tape. A freshly cleaved surface of the gold film was attached to a freshly cleaved WS_2 bulk crystal (CVT crystal from HQ graphene). Gold exfoliation of a large (~1×1 cm^2) bulk WS_2 crystal produces various sizes of continuous single-crystal monolayers up to near the lateral size of the bulk crystal. A gold tape attached on top of a polydimethylsiloxane microlens was used to pick up a part of a single-crystal WS_2 monolayer and reposition it on top of the remaining monolayer after adjusting the twist angle using the tear and stack method[38,39]. This procedure was repeated to produce up to an eight-layer WS_2 stack. A $\langle 0°, 30°, 60°, 90° \rangle$ four-layer WS_2 stack was prepared by picking up part of a bilayer WS_2 stack with an internal twist angle of 30° and placing it on top of the remaining bilayer after 60° rotation. Similarly, we fabricate a two-unit-cell eight-layer stack by lifting and stacking a four-layer stack without rotation. Supplementary Fig. 6 shows the optical microscopy images of the four-layer and eight-layer stacks. Twisted angles of each stack are estimated by polarization-resolved SHG, showing the uncertainty of approximately ±1° from the target twist angles. The uncertainty of twist angles can cause an uncertainty of ~3% in the estimated $\chi^{(2)}_{s,xyz}$ value, which is small compared with the measurement uncertainty (Supplementary Table 3).

Details of nonlinear optical measurements

An optical parametric oscillator (OPO from Light Conversion) with a wavelength of 1,030 nm, repetition frequency of 75 MHz and pulse duration of 96 fs was used to measure the SHG responses for all samples. The SHG signals of twisted bilayer (Fig. 2), trilayer (Fig. 3) and four-layer stacks (Fig. 4b,c) were acquired using the setup shown in Fig. 2a. The sample was mounted on a rotational stage, allowing us to tilt the sample around the x axis and thus to control the incidence angle (β). The setup limits the incident angles up to ±50° that have been used to increase the relative amplitude of the interfacial response with respect to that of the in-plane response. Vertically polarized OPO light was focused onto the tilted sample through an apochromat ×10 objective lens with a numerical aperture of 0.26 (Mitutoyo). The transmitted SHG signals were collected by the same second objective lens, passed through a half-wave plate and horizontal polarizer, and are finally directed to a thermoelectrically cooled 2D charge-coupled device array (iKon-M 912, Andor Technology) equipped with a spectrometer (Kymera 328i, Andor Technology).

For four-layer and eight-layer stacks, imperfect sample preparation can exacerbate distortions of the twist angle. To minimize spatial inhomogeneity, a second setup with a reflective objective lens was used to estimate the normalized $\chi^{(2)}_{s,xyz}$ of the four- and eight-layer stacks (Fig. 4f, purple squares). Transmission SHG is performed using a reflective objective lens (LMM40X-UVV, Thorlabs) with a numerical aperture of 0.5, which enables the simultaneous injections of two oblique incidences at $\beta = \pm 22.5°$ (Supplementary Fig. 5a). The oblique beams are tightly focused onto a spot at a diffraction-limited radius of ~1.3 µm. The transmitted SHG signals were collected by an Apochromat ×20 objective lens with a numerical aperture of 0.4 (Mitutoyo). The SHG signals created by p-polarized injection were selectively collected using a vertically aligned one-dimensional slit and read by the 2D charge-coupled devices (Supplementary Fig. 5b,d). The difference in the SHG signals (Supplementary Fig. 5c,e) is fitted using Supplementary Equation (12), yielding the interfacial sheet susceptibility of the four-layer and eight-layer stacks (Fig. 4f) and minimizing the inhomogeneity effect.

To estimate the excitonic resonance effect of second-order sheet susceptibility elements, we performed SHG measurements using an optical parametric amplifier with a repetition frequency of 3 kHz and a pulse duration of ~180 fs, as well as tuning the excitation wavelength from 1,030 to 1,360 nm. The in-plane sheet susceptibility ($\chi^{(2)}_{s,yyy}$) of a monolayer is estimated from SHG under normal excitation. The interfacial sheet susceptibility ($\chi^{(2)}_{s,xyz}$) of a four-layer stack is estimated by measuring the difference in SHG ($\Delta I_{SHG}/\chi^{(2)}_{s,xxx} \propto \chi^{(2)}_{s,xyz}$) using the setup with a reflective objective lens. Both sheet susceptibility elements are normalized by $\chi^{(2)}_{s,yyy}$ of a monolayer at an excitation of 1,030 nm (Fig. 5). The optical parametric amplifier is tuned to the wavelength of 1,270 nm to perform the THG measurements.

Reporting summary

Further information on research design is available in the Nature Portfolio Reporting Summary linked to this article.

Data availability

The data in the Article are available from the corresponding author upon reasonable request. Source data are provided with this paper.

Acknowledgements

This work was partly supported by the National Science Foundation through the University of Pennsylvania Materials Research Science and Engineering Center DMR-1720530 (B.K.), the US Office of Naval Research (ONR) through grant N00014-20-1-2325 on Robust Photonic Materials with High-Order Topological Protection (B.Z., B.K., J.J., Z.W., L.H. and T.C.) and grant N00014-21-1-2703 (B.Z., B.K., J.J., Z.W., L.H. and T.C.) and the Sloan Foundation (B.Z.). Work by E.J.M. is supported by the Department of Energy under grant DE-FG02-84ER45118. T.C. acknowledges the support of a research grant (project no. 42106) from Villum Fonden.

Author contributions

B.Z. and B.K. conceived the project. B.K. and Z.W. fabricated the twisted stacks. B.K. performed the SHG measurements assisted by J.J. and L.H. B.K. and T.C. performed the symmetry analysis. B.Z., E.J.M. and B.K. discussed and interpreted the results. B.Z. and B.K. wrote the paper with input from all authors. All authors discussed the results.

Competing interests

The authors declare no competing interests.

Additional information

Supplementary information The online version contains supplementary material available at https://doi.org/10.1038/s41566-023-01318-6.

Correspondence and requests for materials should be addressed to Bo Zhen.

Peer review information *Nature Photonics* thanks Wen-Hao Chang and the other, anonymous, reviewer(s) for their contribution to the peer review of this work.

Reprints and permissions information is available at www.nature.com/reprints.

nature portfolio

Corresponding author(s): Bo Zhen
Last updated by author(s): 09/12/2023

Reporting Summary

Nature Portfolio wishes to improve the reproducibility of the work that we publish. This form provides structure for consistency and transparency in reporting. For further information on Nature Portfolio policies, see our Editorial Policies and the Editorial Policy Checklist.

Please do not complete any field with "not applicable" or n/a. Refer to the help text for what text to use if an item is not relevant to your study.
For final submission: please carefully check your responses for accuracy; you will not be able to make changes later.

Statistics

For all statistical analyses, confirm that the following items are present in the figure legend, table legend, main text, or Methods section.

n/a	Confirmed	
☐	☑	The exact sample size (*n*) for each experimental group/condition, given as a discrete number and unit of measurement
☐	☑	A statement on whether measurements were taken from distinct samples or whether the same sample was measured repeatedly
☑	☐	The statistical test(s) used AND whether they are one- or two-sided *Only common tests should be described solely by name; describe more complex techniques in the Methods section.*
☑	☐	A description of all covariates tested
☑	☐	A description of any assumptions or corrections, such as tests of normality and adjustment for multiple comparisons
☐	☑	A full description of the statistical parameters including central tendency (e.g. means) or other basic estimates (e.g. regression coefficient) AND variation (e.g. standard deviation) or associated estimates of uncertainty (e.g. confidence intervals)
☑	☐	For null hypothesis testing, the test statistic (e.g. *F*, *t*, *r*) with confidence intervals, effect sizes, degrees of freedom and *P* value noted *Give P values as exact values whenever suitable.*
☑	☐	For Bayesian analysis, information on the choice of priors and Markov chain Monte Carlo settings
☑	☐	For hierarchical and complex designs, identification of the appropriate level for tests and full reporting of outcomes
☑	☐	Estimates of effect sizes (e.g. Cohen's *d*, Pearson's *r*), indicating how they were calculated

Our web collection on statistics for biologists contains articles on many of the points above.

Software and code

Policy information about availability of computer code

Data collection

Data analysis

For manuscripts utilizing custom algorithms or software that are central to the research but not yet described in published literature, software must be made available to editors and reviewers. We strongly encourage code deposition in a community repository (e.g. GitHub). See the Nature Portfolio guidelines for submitting code & software for further information.

Data

Policy information about availability of data

All manuscripts must include a data availability statement. This statement should provide the following information, where applicable:

- Accession codes, unique identifiers, or web links for publicly available datasets
- A description of any restrictions on data availability
- For clinical datasets or third party data, please ensure that the statement adheres to our policy

The data within this paper are available from the corresponding author upon reasonable request. Source data are provided along with this paper.

Research involving human participants, their data, or biological material

Policy information about studies with human participants or human data. See also policy information about sex, gender (identity/presentation), and sexual orientation and race, ethnicity and racism.

Reporting on sex and gender	
Reporting on race, ethnicity, or other socially relevant groupings	
Population characteristics	
Recruitment	
Ethics oversight	

Note that full information on the approval of the study protocol must also be provided in the manuscript.

Field-specific reporting

Please select the one below that is the best fit for your research. If you are not sure, read the appropriate sections before making your selection.

☐ Life sciences ☐ Behavioural & social sciences ☐ Ecological, evolutionary & environmental sciences

For a reference copy of the document with all sections, see nature.com/documents/nr-reporting-summary-flat.pdf

Life sciences study design

All studies must disclose on these points even when the disclosure is negative.

Sample size	
Data exclusions	
Replication	
Randomization	
Blinding	

Behavioural & social sciences study design

All studies must disclose on these points even when the disclosure is negative.

Study description	
Research sample	
Sampling strategy	
Data collection	
Timing	
Data exclusions	
Non-participation	
Randomization	

Ecological, evolutionary & environmental sciences study design

All studies must disclose on these points even when the disclosure is negative.

Study description

Research sample

Sampling strategy

Data collection

Timing and spatial scale

Data exclusions

Reproducibility

Randomization

Blinding

Did the study involve field work? ☐ Yes ☐ No

Field work, collection and transport

Field conditions

Location

Access & import/export

Disturbance

Reporting for specific materials, systems and methods

We require information from authors about some types of materials, experimental systems and methods used in many studies. Here, indicate whether each material, system or method listed is relevant to your study. If you are not sure if a list item applies to your research, read the appropriate section before selecting a response.

Materials & experimental systems

n/a	Involved in the study
☑	☐ Antibodies
☑	☐ Eukaryotic cell lines
☑	☐ Palaeontology and archaeology
☑	☐ Animals and other organisms
☑	☐ Clinical data
☑	☐ Dual use research of concern
☑	☐ Plants

Methods

n/a	Involved in the study
☑	☐ ChIP-seq
☑	☐ Flow cytometry
☑	☐ MRI-based neuroimaging

Antibodies

Antibodies used

Validation

Eukaryotic cell lines

Policy information about cell lines and Sex and Gender in Research

Cell line source(s)	
Authentication	
Mycoplasma contamination	
Commonly misidentified lines (See ICLAC register)	

Palaeontology and Archaeology

Specimen provenance	
Specimen deposition	
Dating methods	

☐ Tick this box to confirm that the raw and calibrated dates are available in the paper or in Supplementary Information.

Ethics oversight	

Note that full information on the approval of the study protocol must also be provided in the manuscript.

Animals and other research organisms

Policy information about studies involving animals; ARRIVE guidelines recommended for reporting animal research, and Sex and Gender in Research

Laboratory animals	
Wild animals	
Reporting on sex	
Field-collected samples	
Ethics oversight	

Note that full information on the approval of the study protocol must also be provided in the manuscript.

Clinical data

Policy information about clinical studies

All manuscripts should comply with the ICMJE guidelines for publication of clinical research and a completed CONSORT checklist must be included with all submissions.

Clinical trial registration	
Study protocol	
Data collection	
Outcomes	

Dual use research of concern

Policy information about dual use research of concern

Hazards

Could the accidental, deliberate or reckless misuse of agents or technologies generated in the work, or the application of information presented in the manuscript, pose a threat to:

No	Yes	
☑	☐	Public health
☑	☐	National security
☑	☐	Crops and/or livestock
☑	☐	Ecosystems
☑	☐	Any other significant area

Experiments of concern

Does the work involve any of these experiments of concern:

No	Yes	
☑	☐	Demonstrate how to render a vaccine ineffective
☑	☐	Confer resistance to therapeutically useful antibiotics or antiviral agents
☑	☐	Enhance the virulence of a pathogen or render a nonpathogen virulent
☑	☐	Increase transmissibility of a pathogen
☑	☐	Alter the host range of a pathogen
☑	☐	Enable evasion of diagnostic/detection modalities
☑	☐	Enable the weaponization of a biological agent or toxin
☑	☐	Any other potentially harmful combination of experiments and agents

Plants

Seed stocks	
Novel plant genotypes	
Authentication	

ChIP-seq

Data deposition

☐ Confirm that both raw and final processed data have been deposited in a public database such as GEO.

☐ Confirm that you have deposited or provided access to graph files (e.g. BED files) for the called peaks.

Data access links *May remain private before publication.*	
Files in database submission	
Genome browser session (e.g. UCSC)	

Methodology

Replicates	
Sequencing depth	
Antibodies	
Peak calling parameters	
Data quality	
Software	

Flow Cytometry

Plots

Confirm that:

☐ The axis labels state the marker and fluorochrome used (e.g. CD4-FITC).

☐ The axis scales are clearly visible. Include numbers along axes only for bottom left plot of group (a 'group' is an analysis of identical markers).

☐ All plots are contour plots with outliers or pseudocolor plots.

☐ A numerical value for number of cells or percentage (with statistics) is provided.

Methodology

Sample preparation

Instrument

Software

Cell population abundance

Gating strategy

☐ Tick this box to confirm that a figure exemplifying the gating strategy is provided in the Supplementary Information.

Magnetic resonance imaging

Experimental design

Design type

Design specifications

Behavioral performance measures

Imaging type(s)

Field strength

Sequence & imaging parameters

Area of acquisition

Diffusion MRI ☐ Used ☐ Not used

Preprocessing

Preprocessing software

Normalization

Normalization template

Noise and artifact removal

Volume censoring

Statistical modeling & inference

Model type and settings

Effect(s) tested

Specify type of analysis: ☐ Whole brain ☐ ROI-based ☐ Both

Statistic type for inference

(See Eklund et al. 2016)

Correction

Models & analysis

n/a	Involved in the study
☑	☐ Functional and/or effective connectivity
☑	☐ Graph analysis
☑	☐ Multivariate modeling or predictive analysis

Functional and/or effective connectivity

Graph analysis

Multivariate modeling and predictive analysis